

# Thermal-Field Electron Emission from Three-Dimensional Topological Semimetals

Wei Jie Chan,<sup>1</sup> Yee Sin Ang,<sup>1,\*</sup> and L. K. Ang<sup>1,†</sup>

<sup>1</sup>*Science, Mathematics and Technology (SMT), Singapore University of Technology and Design (SUTD), 8 Somapah Road, Singapore 487372*

A model is constructed to describe the thermal-field emission of electrons from a three-dimensional (3D) topological semimetal hosting Dirac/Weyl node(s). The traditional thermal-field electron emission model is generalised to accommodate the 3D non-parabolic energy band structures in the topological Dirac/Weyl semimetals, such as cadmium arsenide ( $\text{Cd}_3\text{As}_2$ ), sodium bismuthide ( $\text{Na}_3\text{Bi}$ ), tantalum arsenide ( $\text{TaAs}$ ) and tantalum phosphide ( $\text{TaP}$ ). Due to the unique Dirac cone band structure, an unusual dual-peak feature is observed in the total energy distribution (TED) spectrum. This non-trivial dual-peak feature, absent from traditional materials, plays a critical role in manipulating the TED spectrum and the magnitude of the emission current. At zero temperature limit, a new scaling law for pure field emission is derived and it is different from the well-known Fowler-Nordheim (FN) law. This model expands the recent understandings of electron emission studied for the Dirac 2D materials into the 3D regime, and thus offers a theoretical foundation for the exploration in using topological semimetals as novel electrodes.

## I. INTRODUCTION

Topological Weyl/Dirac semimetals (WSM/DSM)s, a subset of Dirac materials have been studied rapidly over the past decade [1–9] due to its electronic [10–13], optical [13–16] and magnetic [13, 16, 17] properties. The unconventional band structures about its Dirac point have brought about many interesting applications in electronics [18–20], spintronics [21], photonics [22, 23], nonlinear optics [24–26] and topological electronics (topotronics) [27]. Apart from these applications, the physics of electron emission from Dirac materials like carbon-based nanomaterials [28–30] or graphene [31–40] have also received attentions over the past two decades.

Field-induced electron emission describes the quantum tunnelling of electrons from a material surface into a vacuum under a strong electric field. The most well-known field emission physics is described by the Fowler-Nordheim (FN) based models developed for traditional bulk materials [41–43]. Compared to the conventional field emitters [44–49], novel quantum materials exhibit Dirac conic band structure about its Fermi level with non-parabolic energy dispersion [9], and they have also been experimentally shown to exhibit large field enhancement and stable current emission [50–52]. However, the physics of thermal-field emission of some recently discovered topological solids (such as 3D Dirac/Weyl semimetals) has not been studied in details, which immediately leads to the following questions: (i) How can the conventional thermal-field emission model be generalized to accommodate the nonparabolic band structure of topological semimetals? (ii) How does the Dirac conic band structure affect the thermal-field emission behaviours of 3D WSM/DSM? (iii) What are the differences between

conventional metal and WSM/DSM in terms of their current, voltage and temperature scaling laws at the both field and thermal-field emission regimes?

In this paper, we address the above questions by constructing a generalized thermal-field emission model for the newly discovered 3D DSMs/WSMs. In particular, the total energy distribution (TED) and the emission current density are calculated. Our model applies the Dirac cone approximation for DSMs/WSMs and considers the Schottky-Nordheim (SN) barrier [41, 53] at the material-vacuum interface, as seen in Fig. 1(a). The electron emission can reside from either the conduction (orange) or valence (blue) bands and are then replenished (purple) at the intrinsic Fermi level,  $\varepsilon_{F0}$ . The differing (linear) energy dispersion from a Dirac cone allows us to study the thermal-field emission of 3D DSMs/WSMs. For a linear dispersion, we predict an unconventional TED behaviour and a new  $F^3$  scaling law at the zero temperature limit, which is different from the FN law. By tuning the applied electric field strength, temperature and Fermi level of a DSM/WSM, we can manipulate the energy profile of TED and the magnitude of the emission current density. These findings can pave the way for the theoretical study of other topological materials, in particular, materials that are described by Dirac cone(s) and Weyl nodes in the band structure, which cannot be modelled by the traditional thermal-field emission models [53].

## II. THERMAL-FIELD EMISSION MODELS

We consider a generalized thermal-field electron emission model in the form of

$$\mathcal{J}_\perp = \frac{eg}{(2\pi)^3} \int v_\perp(\varepsilon_{\mathbf{k}}) \Theta(k_\perp) f(\varepsilon_{\mathbf{k}}) \mathcal{T}(\varepsilon_\perp) d^3\mathbf{k}, \quad (1)$$

where  $\mathcal{J}_\perp$  is the electron current density emitted vertically from a surface,  $e$  is the charge of an electron,  $g$  is

\* yeesin\_ang@sutd.edu.sg

† ricky\_ang@sutd.edu.sg

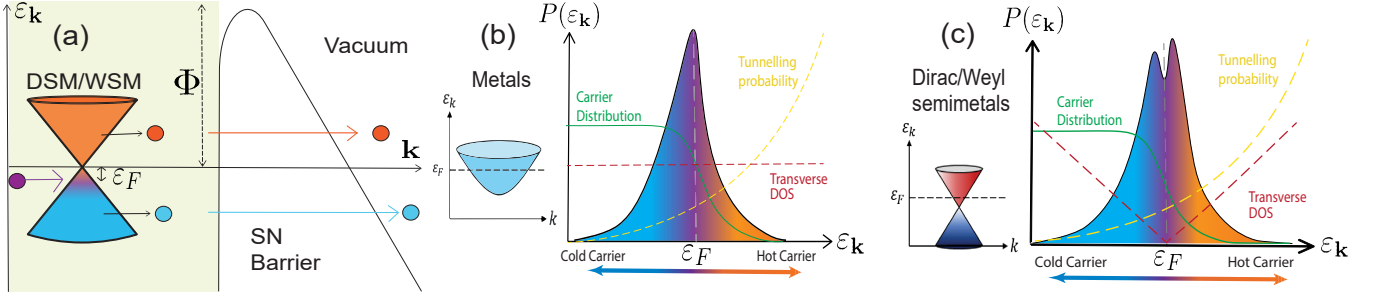


FIG. 1: (a) Schematic diagram of a material with a linear dispersion under the Dirac cone approximation. Under an electric field, the electrons emit through a Schottky-Nordheim (SN) barrier [53] with work function,  $\Phi$ , into vacuum. Orange/blue electrons are emitted respectively, from the conduction/valence bands. The emitted electrons are then replenished at the Fermi level,  $\varepsilon_F$  immediately by replacement electrons (purple) entering the Dirac cone [46]. The relationship of the energy dispersion, carrier density (green solid line), tunnelling probability (yellow dotted line), and in particular, the transverse density of states (DOS) (red dotted line), help sculpt the total energy distribution (TED),  $P(\varepsilon_{\mathbf{k}})$  of (b) a conventional metal with a parabolic dispersion, giving us a single peak TED, and (c) of a DSM/WSM using the Dirac cone approximation, giving us a dual-peak feature in the TED.

the degeneracy factor,  $f(\varepsilon_{\mathbf{k}})$  is the Fermi-Dirac distribution function and  $\mathcal{T}(\varepsilon_{\perp})$  is the tunnelling probability. The Heaviside step function,  $\Theta(k_{\perp})$ , is defined to exclude the electronic states propagating backward in the negative vertical  $\perp$  direction. The group velocity along the emitting direction (denoted as  $\perp$ ) is

$$v_{\perp}(\varepsilon_{\mathbf{k}}) = \frac{1}{\hbar} \frac{\partial \varepsilon_{\mathbf{k}}}{\partial |k_{\perp}|}. \quad (2)$$

In the following, we define  $\perp$  to be pointing in the  $z$  direction and  $\parallel$  along the  $x$ - $y$  plane. The tunnelling probability  $\mathcal{T}$  in Eq. (1) can be modelled after the SN barrier model [41, 53] to account for the image charge potential, given by

$$\mathcal{T}(\varepsilon_{\perp}) \approx \mathcal{D}_F \exp\left\{\frac{\varepsilon_{\perp} - \varepsilon_F}{d_F}\right\}, \quad (3)$$

where  $\mathcal{D}_F \equiv \exp(-bv\sqrt{\Phi^3}/F)$  is the tunnelling exponent term and  $d_F \equiv 2F/3b\sqrt{\Phi}\tau$  is the decay width of the wave function through the barrier,  $b = 4\sqrt{2m}/3e\hbar$  is a Fowler-Nordheim (FN) constant [42] with  $m$  being the electron mass,  $\Phi$  is the work function of the material, and  $F$  is the applied field. The image charge effect can be approximated with the following correction terms: [41]

$$v \approx 1 - f_s + \frac{f_s}{6} \ln f_s, \quad \tau \approx 1 + \frac{f_s}{9} - \frac{f_s}{18} \ln f_s, \quad (4)$$

with  $f_s = e^3 F/4\pi\epsilon_0\Phi^2$ , where  $\epsilon_0$  is the vacuum permittivity.

### A. Generalized thermal-field emission current density for non-parabolic energy dispersion

To accommodate the non-parabolic energy dispersion, we transform Eq. (1) into an alternative form. We first consider a generic energy dispersion,  $\varepsilon_{\mathbf{k}}(\varepsilon_{\parallel}(\mathbf{k}_{\parallel}), \varepsilon_{\perp}(\mathbf{k}_{\perp}))$  with  $\varepsilon_{\parallel}(\mathbf{k}_{\parallel})$  and  $\varepsilon_{\perp}(\mathbf{k}_{\perp})$  as the energy component transverse and along the tunnelling direction, respectively. By rewriting Eq. (1) in terms of the  $\perp$  and the  $\parallel$  components through  $d^3\mathbf{k} = k_{\parallel}dk_{\parallel}d\phi_{\mathbf{k}_{\parallel}}dk_{\perp}$ , with  $\phi_{\mathbf{k}_{\parallel}} = \tan^{-1}(k_y/k_x)$ , we have

$$\begin{aligned} \mathcal{J}_{\perp} &= \frac{e}{2\pi\hbar} \left( \int f(\varepsilon_{\mathbf{k}}) \mathcal{T}(\varepsilon_{\perp}) \Lambda_{\perp} d\varepsilon_{\perp} \right) \\ &\times \left( \iint \frac{g}{(2\pi)^2} \Lambda_{\parallel}^{-1} d\phi_{\mathbf{k}_{\parallel}} d\varepsilon_{\parallel} \right), \end{aligned} \quad (5)$$

where we have defined the energy dispersion factors as

$$(\Lambda_{\perp}, \Lambda_{\parallel}) \equiv \left( \frac{\partial \varepsilon_{\mathbf{k}}}{\partial |\varepsilon_{\perp}|}, \frac{1}{k_{\parallel}} \frac{d\varepsilon_{\parallel}}{dk_{\parallel}} \right), \quad (6)$$

and the following transformation identity is used

$$\frac{\partial \varepsilon_{\mathbf{k}}}{\partial |k_{\perp}|} \mathbf{k}_{\parallel} dk_{\parallel} dk_{\perp} = \frac{\partial \varepsilon_{\mathbf{k}}}{\partial |\varepsilon_{\perp}|} d\varepsilon_{\perp} \frac{k_{\parallel}}{\partial \varepsilon_{\parallel} / \partial k_{\parallel}} d\varepsilon_{\parallel}.$$

Note that  $k_{\parallel} = k_{\parallel}(\varepsilon_{\parallel}, \phi_{\mathbf{k}_{\parallel}})$  is defined. The energy dispersion factors in Eq. (6) play crucial roles in understanding the electron field emission with non-parabolic energy dispersion.

Consider an isotropic 3D parabolic energy dispersion,  $\varepsilon_{\mathbf{k}} = \hbar^2(k_{\parallel}^2 + k_{\perp}^2)/2m^*$  where  $m^*$  is the electron effective mass and  $\mathbf{k} = (\mathbf{k}_{\parallel}, \mathbf{k}_{\perp})$  with  $\mathbf{k}_{\parallel}$  representing the wave vector component transverse to the emission direction, the total energy is *partitioned* into the emission

TABLE I: Material parameters of the DSM: Cd<sub>3</sub>As<sub>2</sub> and Na<sub>3</sub>Bi, and WSMs: TaAs and TaP, are listed in this table. The parameters consists of the work function,  $\Phi$ , the intrinsic Fermi level,  $\varepsilon_{F0}$ , the Fermi velocities in the transverse direction,  $v_{Fx}$  and  $v_{Fy}$  and, the degeneracies of the nodes in the dispersion space,  $g$ . WSMs must have at least a pair of distinct Weyl nodes [9].

DSMs/WSMs	$\Phi$ (eV)	$\varepsilon_{F0}$ (eV)	$v_{Fx}$ (10 <sup>6</sup> m/s)	$v_{Fy}$ (10 <sup>6</sup> m/s)	$g$
Cd <sub>3</sub> As <sub>2</sub> <sup>a</sup>	4.5	0.1	1.3	1.28	4
Na <sub>3</sub> Bi <sup>b</sup>	2.35	0.025	0.374	0.374	4
TaAs <sup>c</sup>	4.65	-0.0221, -0.0089	0.292, 0.2055	0.1532, 0.1579	8, 16
TaP <sup>d</sup>	5.405	-0.0531, 0.0196	0.327, 0.3736	0.1594, 0.2542	8, 16

<sup>a</sup> References [6, 8, 54, 55]

<sup>b</sup> References [7, 54]

<sup>c</sup> References [56–58]

<sup>d</sup> References [56, 58]

component  $\varepsilon_{\perp} \equiv \hbar^2 k_{\perp}^2 / 2m^*$ , the transverse component  $\varepsilon_{\parallel} \equiv \hbar^2 k_{\parallel}^2 / 2m^*$ , and  $\varepsilon_{\mathbf{k}} = \varepsilon_{\parallel} + \varepsilon_{\perp}$ . In doing so, Eq. (6) becomes

$$(\Lambda_{\perp}, \Lambda_{\parallel})^{\text{parabolic}} \equiv \left(1, \frac{\hbar^2}{m^*}\right), \quad (7)$$

which is a constant term (independent of  $\varepsilon_{\parallel}$  and  $\varepsilon_{\perp}$ ). Solving Eq. (1) with Eq. (7) will yield the classic Fowler-Nordheim (FN) law for cold field emission, and the Murphy-Good (MG) model for thermal-field emission.

For a non-parabolic (or linear) energy dispersion, we have

$$\varepsilon_{\mathbf{k}} = \sqrt{\varepsilon_{\mathbf{k}\perp}^2 + \varepsilon_{\mathbf{k}\parallel}^2}. \quad (8)$$

For topological Dirac/Weyl semimetals, the quasiparticles around the Dirac point(s) are described by the effective Hamiltonian,  $\mathcal{H}_{\mathbf{k}} = \hbar \sum_{i,a} v_{Fi,a} k_{i,a} \sigma_i$  where  $i = \{x, y, z\}$  and  $\sigma_i$  is the Pauli matrix along  $\hat{i}$  and the subscript  $a$  labels the  $a$ th Dirac cone [9, 56, 57, 59, 60]. The energy dispersion of these topological semimetals (SM) is

$$\varepsilon_{\mathbf{k}}^{\text{SM}} = \sum_{a=1}^N \sqrt{\sum_i \hbar^2 v_{Fi,a}^2 k_{i,a}^2}, \quad (9)$$

where  $\varepsilon_{\parallel,a} \equiv \hbar (v_{Fx,a} k_{x,a}^2 + v_{Fy,a} k_{y,a}^2)^{1/2}$  and  $\varepsilon_{\perp,a} \equiv \hbar v_{Fz,a} k_{z,a}$ . The corresponding energy dispersion factors for non-parabolic dispersion are

$$(\Lambda_{\perp,a}, \Lambda_{\parallel,a})^{\text{SM}} \equiv \left( \frac{|\varepsilon_{\perp,a}|}{\varepsilon_{\mathbf{k},a}}, \frac{\hbar^2 \tilde{v}_a^2}{\varepsilon_{\parallel,a}} \right), \quad (10)$$

where  $\tilde{v}_a \equiv v_{Fy,a} \sqrt{(v_{Fx,a}/v_{Fy,a})^2 \cos^2 \phi_{\mathbf{k}\parallel} + \sin^2 \phi_{\mathbf{k}\parallel}}$ ,  $a$  is the Fermi velocity along the  $\parallel$  direction. This is in stark contrasts to the parabolic dispersion case as shown in Eq. (7) and will lead to a drastically different thermal-field emission characteristics for topological Dirac/Weyl semimetals to be reported below.

## B. Thermal-field emission current density and total energy distribution from Dirac cones

For an isotropic parabolic energy dispersion, Eq. (5) can be simplified as

$$\mathcal{J}_{\perp}^{\text{parabolic}} = \frac{g_s m e}{(2\pi)^2 \hbar^3} \int f(\varepsilon_{\mathbf{k}}) \mathcal{T}(\varepsilon_{\perp}) d\varepsilon_{\perp} d\varepsilon_{\mathbf{k}}, \quad (11)$$

$g_s$  is the spin degeneracy,  $\frac{\partial \varepsilon_{\mathbf{k}}}{\partial \varepsilon_{\mu}} = 1$ ,  $\mu \in \{\perp, \parallel\}$  which can be approximately solved to yield the well-known Murphy-Good (MG) thermal-field emission model [53]:

$$\mathcal{J}_{\perp}^{\text{MG}} = \frac{a_{\text{FN}} F^2}{\Phi t^2} D_F \frac{k_B T \pi / d_F}{\sin(k_B T \pi / d_F)}, \quad (12)$$

where  $a_{\text{FN}} = e^3 / (16\pi^2 \hbar)$  is the FN constant and  $k_B$  is the Boltzmann constant.

The FN plot (for FN scaling) can be obtained by rearranging Eq. (12) such that,

$$\ln \left( \frac{\mathcal{J}_{\perp}^{\text{MG}}}{F^2} \right) = -\frac{b v \sqrt{\Phi^3}}{F} + \ln \left( \frac{a_{\text{FN}} k_B T \pi / d_F}{\Phi t^2 \sin(k_B T \pi / d_F)} \right). \quad (13)$$

At  $T = 0$  K (cold field emission), it recovers the classical FN scaling of  $\ln(\mathcal{J}_{\perp}^{\text{MG}}/F^2) \propto -1/F$ . Note the  $F^2$  component in the logarithm term is a signature of field emission from bulk materials.

In contrast, Eq. (5) of a DSM/WSM exhibits a non-trivial difference due to Eq. (10), which can be written as

$$\mathcal{J}_{\perp}^{\text{SM}} = \sum_{a=1}^N \frac{g_a e}{(2\pi \hbar)^3} \left( \int |\varepsilon_{\perp,a}| \mathcal{T}(\varepsilon_{\perp,a}) f(\varepsilon_{\mathbf{k},a}) d\varepsilon_{\perp,a} \right) \times \left( \iint \frac{\varepsilon_{\parallel,a}}{\tilde{v}_a^2} d\phi_{\mathbf{k}\parallel,a} d\varepsilon_{\mathbf{k},a} \right), \quad (14)$$

where  $g_a$  is the spin and node degeneracy for each contributing Dirac cone,  $N$  is the number of contributing

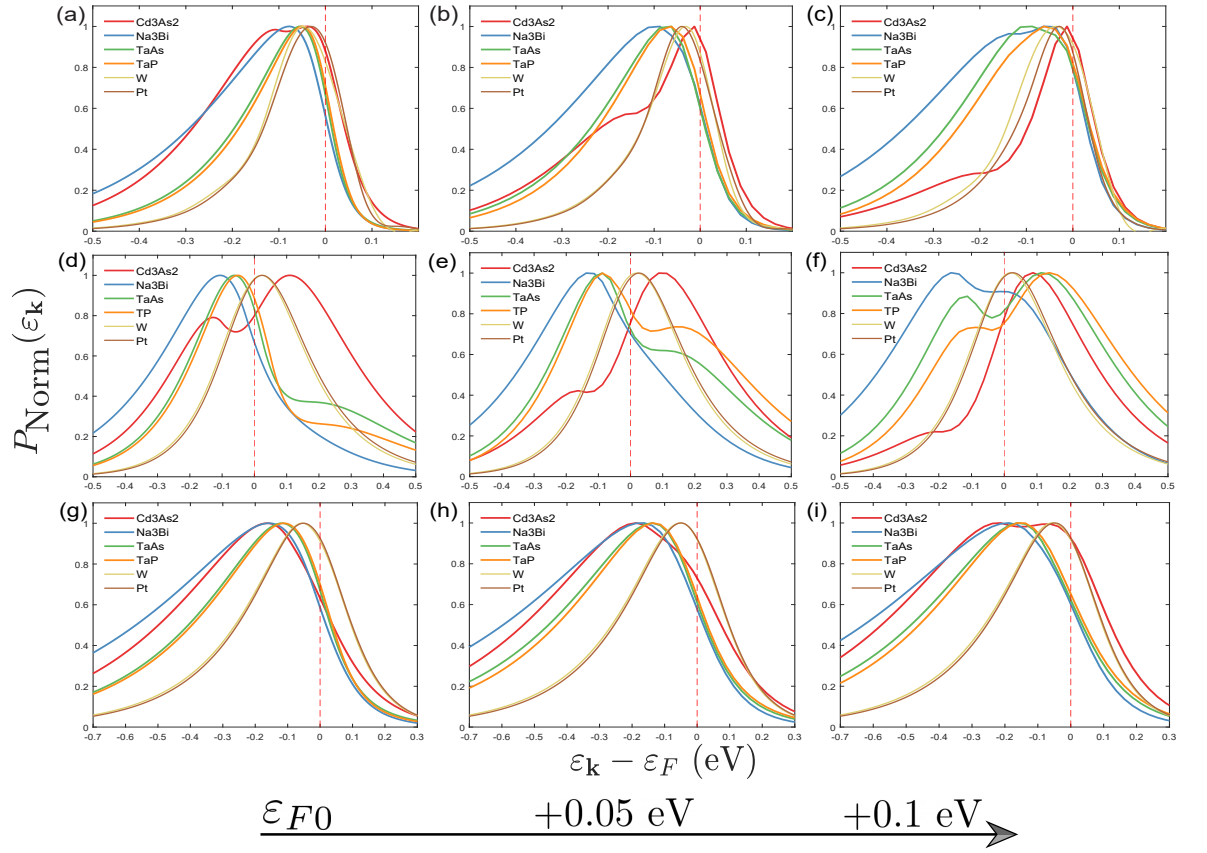


FIG. 2: The normalized (with respect to the maxima) TEDs are shown for  $\text{Cd}_3\text{As}_2$  (red line),  $\text{Na}_3\text{Bi}$  (blue line),  $\text{TaAs}$  (green line),  $\text{TaP}$  (orange line),  $\text{W}$  (yellow line) and  $\text{Pt}$  (brown line) using material parameters in Table I and [49, 61, 62] respectively. The red dotted line indicates the Fermi level. Along each row, the TEDs are plotted under  $T = 300$  K and  $F = 2.5$  V/nm for (a) to (c),  $T = 700$  K and  $F = 2.5$  V/nm for (d) to (f),  $T = 700$  K and  $F = 5$  V/nm for (g) to (i). Along each column, the TEDs are plotted using the intrinsic Fermi level  $\varepsilon_{F0}$  in (a), (d), (g),  $\varepsilon_{F0} + 0.05$  eV in (b), (e), (h), and  $\varepsilon_{F0} + 0.1$  eV in (c), (f), (i). The TEDs are shifted along the  $\varepsilon_{\mathbf{k}}$  axis such that all the Fermi level is zero (red vertical dotted line). The carriers left/right of the Fermi level are from either the valence/conduction band. The dual peak feature can be seen in all DSMs/WSMs, particularly in (d), (e) and (f) as we elevate  $T$  and lower  $F$  to sufficient values. Note the 2 bulk materials ( $\text{W}$  and  $\text{Pt}$ ) will always have single-peak TED

Dirac cone(s) to the emission. Eq. (14) can be further simplified and numerically solved as

$$\mathcal{J}_{\perp}^{\text{SM}} = \sum_{a=1}^N \frac{c_{\text{SM},a} F^2}{\Phi t^2} D_F \exp\left\{-\frac{\varepsilon_F}{d_F}\right\} \times \int_{-\infty}^{\infty} f(\varepsilon_{\mathbf{k},a}) \lambda(\varepsilon_{\mathbf{k},a}/d_F) d\varepsilon_{\mathbf{k},a}, \quad (15)$$

where  $c_{\text{SM},a} = e^3 g_a / (32 m_e \pi^2 \hbar v_{F_x,a} v_{F_y,a})$  is a constant with the rest mass of the electron being  $m_e$  and the dimensionless tunnelling function  $\lambda$  is defined as

$$\lambda(\varepsilon_{\mathbf{k},a}/d_F) = \exp\left\{\frac{\varepsilon_{\mathbf{k},a}}{d_F}\right\} \left(\frac{\varepsilon_{\mathbf{k},a}}{d_F} - 1\right) \text{sign}(\varepsilon_{\mathbf{k},a}) + 1 + \text{sign}(\varepsilon_{\mathbf{k},a}). \quad (16)$$

The FN plot now takes the form of

$$\ln\left(\frac{\mathcal{J}_{\perp}^{\text{SM}}}{F^2}\right) = \sum_{a=1}^N -\frac{bv\sqrt{\Phi^3}}{F} - \frac{\varepsilon_F}{d_F} + \ln\left(\frac{c_{\text{SM},a}}{\Phi t^2}\right) + \ln\left(\int_{-\infty}^{\infty} f(\varepsilon_{\mathbf{k},a}) \lambda(\varepsilon_{\mathbf{k},a}/d_F) d\varepsilon_{\mathbf{k},a}\right). \quad (17)$$

At  $T = 0$  K (cold field emission), Eq. (15) becomes

$$\mathcal{J}_{\perp}^{\text{SM}}(T = 0) = \sum_{a=1}^N \frac{2c_{\text{SM},a} \sqrt{\Phi} D_F}{3b_{FN} t^2} \left(2\Gamma_- + \frac{\varepsilon_F}{d_F} \Gamma_+\right) F^3, \quad (18)$$

where  $\Gamma_{\pm} = 2 \exp\{-\varepsilon_F/d_F\} \pm 1$ . The scaling law at

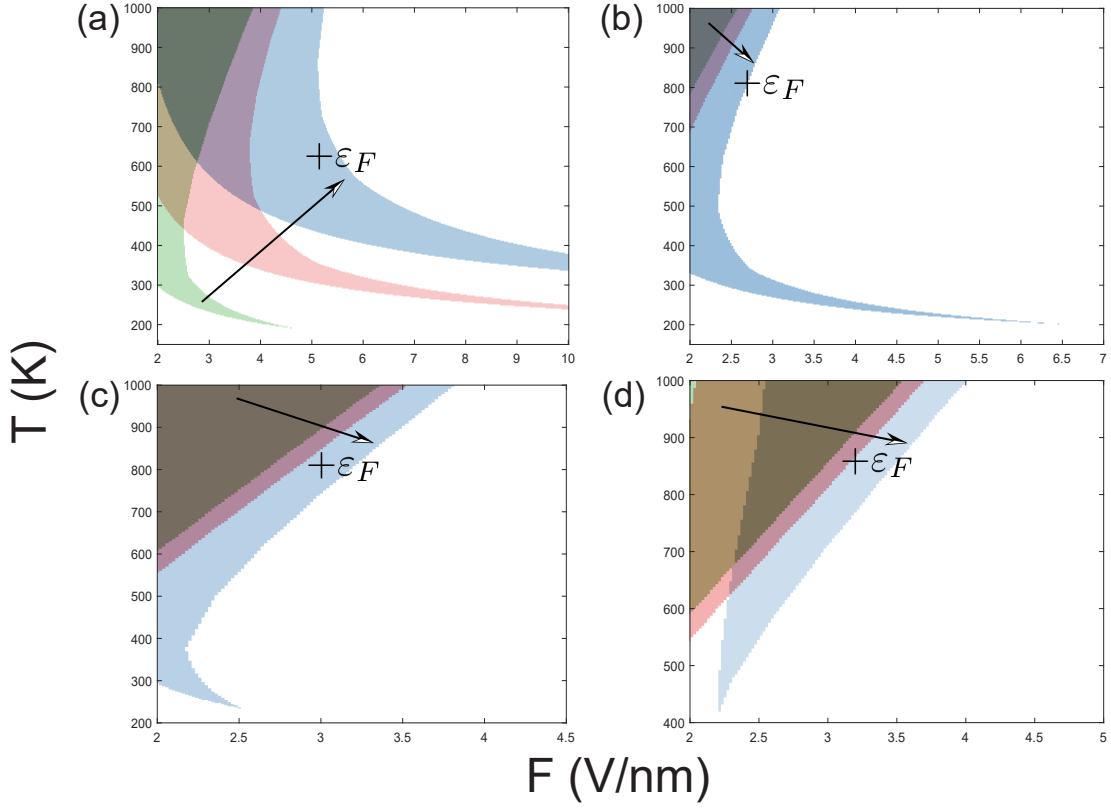


FIG. 3: The TED peak diagrams are shown for (a)  $\text{Cd}_3\text{As}_2$ , (b)  $\text{Na}_3\text{Bi}$ , (c)  $\text{TaAs}$ , and (d)  $\text{TaP}$  based on the material parameters in Table I. The coloured regions are the regions with dual-peak feature at different Fermi energy level from the intrinsic value  $\varepsilon_{F0}$  in (green region) to  $\varepsilon_{F0} + 0.05$  eV (red region) and  $\varepsilon_{F0} + 0.1$  eV (blue region). The white (uncoloured) regions are parameters that does not exhibit the dual peak feature.

$T = 0$  then becomes

$$\ln\left(\frac{\mathcal{J}_{\perp}^{\text{SM}}(T=0)}{F^3}\right) = \sum_{a=1}^N -\frac{bv\sqrt{\Phi^3}}{F} + \ln\left(\frac{2c_{\text{SM},a}\sqrt{\Phi}}{3b_{\text{FN}}t^3}\right) + \ln\left(2\Gamma_{-} + \frac{\varepsilon_F}{d_F}\Gamma_{+}\right), \quad (19)$$

where  $\Gamma_{\pm}$  is negligible in the pure field emission regime. Thus this produces an unexpected scaling of

$$\ln\left(\frac{\mathcal{J}_{\perp}^{\text{SM}}}{F^3}\right) \propto -\frac{1}{F}, \quad (20)$$

which is different from the classical FN scaling of  $\ln(\mathcal{J}_{\perp}^{\text{MG}}/F^2) \propto -1/F$  for bulk solids with parabolic dispersion.

The energy spectrum of the emitted electrons is determined from the total energy distribution (TED):  $P(\varepsilon_{\mathbf{k}})$  by considering  $\partial\mathcal{J}_{\perp}/\partial\varepsilon_{\mathbf{k}}$  such that,

$$P(\varepsilon_{\mathbf{k}}) = \frac{e}{2\pi\hbar^3} f(\varepsilon_{\mathbf{k}}) \int \mathcal{T}(\varepsilon_{\perp}) \Lambda_{\perp} D(\varepsilon_{\mathbf{k}}) d\varepsilon_{\perp} d\phi_{\mathbf{k}_{\parallel}}, \quad (21)$$

where the transverse density of states is  $\int D(\varepsilon_{\parallel}) d\phi_{\mathbf{k}_{\parallel}} d\varepsilon_{\parallel} = \int D(\varepsilon_{\mathbf{k}}) d\phi_{\mathbf{k}_{\parallel}} d\varepsilon_{\mathbf{k}}$ , with  $D(\varepsilon_{\mathbf{k}}) = g/((2\pi)^2 \Lambda_{\parallel}(\varepsilon_{\mathbf{k}}))$ .

For a parabolic dispersion, the TED takes on a conventional single peak behaviour due to the trivial energy dispersion factors in Eq. (7), which gives us the well-known MG TED in the form of,

$$P^{\text{MG}}(\varepsilon_{\mathbf{k}}) = c_T \frac{F}{\sqrt{\Phi} t} D_F f(\varepsilon_{\mathbf{k}}) \exp\left\{\frac{\varepsilon_{\mathbf{k}} - \varepsilon_F}{d_F}\right\}. \quad (22)$$

On the contrary, Eq. (10) will produce a differing and non-trivial ( $\varepsilon_{\parallel}$  and  $\varepsilon_{\perp}$  dependence) term in the transverse DOS and the  $\varepsilon_{\perp}$  integration, which is

$$P^{\text{SM}}(\varepsilon_{\mathbf{k}}) = \sum_{a=1}^N \frac{c_{\text{SM},a} F^2}{\Phi t^2} D_F \exp\left\{-\frac{\varepsilon_F}{d_F}\right\} \times f(\varepsilon_{\mathbf{k},a}) \lambda(\varepsilon_{\mathbf{k},a}/d_F). \quad (23)$$

Unlike the parabolic dispersion commonly used for bulk metals in Fig. 1(b), the linear dispersion and the vanishing density of states of a DSM/WSM portrays a new dual-peak feature in the TED, as illustrated in Fig. 1(c). This distinctive feature is attributed by the products of three terms in Eq. (21):  $f(\varepsilon_{\mathbf{k}})$  (green solid line), the  $\varepsilon_{\perp}$  integration of  $\Lambda_{\perp} \mathcal{T}(\varepsilon_{\perp})$  (yellow dotted line), and the  $\phi_{\mathbf{k}_{\parallel}}$  integration of  $D(\varepsilon_{\parallel})$  (red dotted line). The

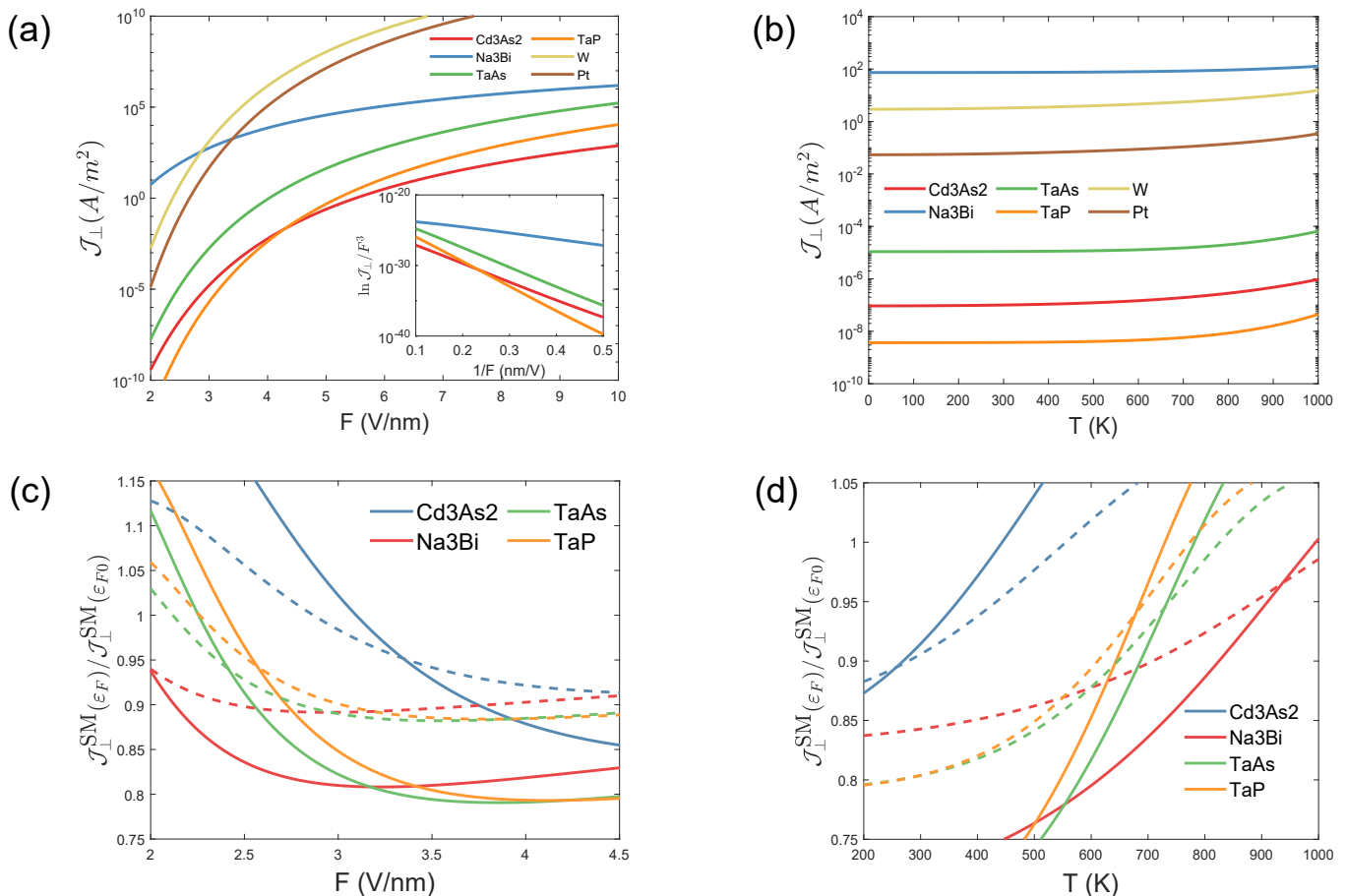


FIG. 4: Thermal-field emission current density at (a)  $T = 700$  K with varying  $F$ , and (b)  $F = 2.5$  V/nm with varying  $T$ , for 6 materials: Tungsten (W), Platinum (Pt),  $\text{Cd}_3\text{As}_2$ ,  $\text{Na}_3\text{Bi}$ , TaAs and TaP. The inset in (a) shows the unconventional  $F^3$  scaling law in the FN plots for DSMs/WSMs. (b) The ratio of the emission current density at enhanced Fermi energy level ( $\varepsilon_F$ ) to that at intrinsic level ( $\varepsilon_{F0}$ ) at (c)  $T = 700$  K with varying  $F$  and (d) at  $F = 2.5$  V/nm with varying  $T$ . The dashed and solid lines corresponds to the enhanced  $\varepsilon_F$  of 0.05 eV and 0.1 eV, respectively.

coloured region under the TED graph corresponds to the emitting energy band, where blue/orange represents the emission from the valence/conduction band. The purple region represents the emission around the Fermi level. As seen below, this unconventional behaviour in the TED can be utilised to manipulate the energy profile of the emission process.

### III. RESULTS AND DISCUSSION

#### A. Dual-peak total energy distribution

We investigate the appearance of the dual-peak feature in 4 topological semimetals in Fig. 2. The material parameters for the topological semimetals are given in Table I. In comparison, 2 bulk metals [49, 61, 62] are considered in our calculations: (a) Tungsten W with  $\Phi = 5.25$

eV and  $\varepsilon_{F0} = 11.55$  eV; (b) Platinum Pt with  $\Phi = 5.65$  eV and  $\varepsilon_{F0} = 8.78$  eV. Unlike topological semimetals, materials modelled with a parabolic dispersion like W and Pt do not generate this dual-peak behaviour in its TED for all ranges of  $F$ ,  $T$  and  $\varepsilon_F$ . This behaviour arises in topological semimetals from  $P^{\text{SM}}(\varepsilon_{\mathbf{k}}) \propto \lambda(\varepsilon_{\mathbf{k}}/d_F)$  in Eq. (23) due to the differing (Dirac conic) band structure embedded in Eq. (10). In contrast, this is not seen for a parabolic dispersion as  $P^{\text{MG}}(\varepsilon_{\mathbf{k}}) \propto \exp\{\varepsilon_{\mathbf{k}}/d_F\}$  in Eq. (22) from Eq. (7) and is consistent with Figs. 1(b) and 1(c). The dual-peak TED is thus a signature of the Dirac conic band structure.

Furthermore, the dual-peak feature can be generated or removed by regulating the energies of the carriers by changing  $T$  and  $F$ . This can be seen by comparing Figs. 2(a) to 2(c) ( $T = 300$  K,  $F = 2.5$  V/nm) and Figs. 2(g) to 2(i) ( $T = 700$  K,  $F = 5$  V/nm) against Figs. 2(d) to 2(f) ( $T = 700$  K,  $F = 2.5$  V/nm). The



dependency of  $f(\varepsilon_{\mathbf{k}})$  in Eq. (23) regulates the number of high energy carriers (from the conduction band) as  $T$  is varied. As the height of the potential barrier is varied through  $F$ , the dependency of  $D_F \lambda(\varepsilon_{\mathbf{k}}/d_F)$  in Eq. (23) makes it easier/harder for the low energy carriers (from the valence band) to tunnel across the surface barrier. Hence, the dual-peak feature can be modulated by tuning the  $F$  and  $T$  until the number of high and low energy carriers for emission is similar/vastly different. This feature appears in Fig. 2(d) for  $\text{Cd}_3\text{As}_2$  (red line), with the peak before/after the Fermi level (red dotted line) termed as the low/high energy peak. Likewise, the dual peaks disappear as  $F$  is further increased, allowing more low energy carriers to be emitted as shown in  $\text{Cd}_3\text{As}_2$  [Fig. 2(f)]. Thus, the dual-peak feature is not robust against the variation of  $T$  and  $F$ .

In addition to  $F$  and  $T$ , the dual-peaks can also be created by varying  $\varepsilon_F$ . This can be seen across the columns of Fig. 2, that an increase of  $\varepsilon_F$  introduces more hot carriers. This is supported by Eq. (23), where the  $f(\varepsilon_{\mathbf{k}})$  term introduce more hot carriers and the  $\exp\{-\varepsilon_F/d_F\} \lambda(\varepsilon_{\mathbf{k}}/d_F)$  term allows the hot carriers to tunnel through easier from increasing  $\varepsilon_F$ . An explicit example can be seen in Figs. 2(e) and 2(f) for  $\text{Na}_3\text{Bi}$  (blue line), where the dual-peak feature appears only after a sufficient increased of  $\varepsilon_F$ . Hence, the  $\varepsilon_F$  plays a vital role in regulating the number of hot carriers for emission, which is crucial in manipulating the dual-peak feature.

## B. Susceptibility diagram of the dual-peak TED

In Fig. 3, we further study the mechanism of the dual-peak feature in Fig. 2 as illustrated by increasing  $\varepsilon_F$  in the susceptibility ( $F$ - $T$ ) diagram of the dual-peak feature. It can be seen that the dual-peak regions expand and shift with increasing  $\varepsilon_F$  in all four topological semimetals. This is predicted in Eq. (23) and Fig. 2, where the increase in  $\varepsilon_F$  increases the number of high energy carriers. Due to the scarcity of the high energy carriers in the field emission regime, the expansion of the region is expected as the increased number of high energy carriers makes it more conducive to generate the dual-peak feature by the variation of  $F$  and  $T$ , which is seen in Figs. 3(b) and 3(c) for  $\text{Na}_3\text{Bi}$  and  $\text{TaAs}$ . The shifting of the regions indicates that the dual-peak feature can be generated or removed at different ranges of  $F$  and  $T$ , with an increasing number of high energy carriers by increasing  $\varepsilon_F$ . This is explicitly seen in Figs. 3(a) and 3(d) for  $\text{Cd}_3\text{As}_2$  and  $\text{TaP}$  and is supported by the gain or loss of the dual-peak feature in Fig. 2. Thus, the susceptibility diagram pinpoints the parameters to achieve the dual-peak feature, which can be useful in generating a larger emission current density as seen in Fig. 4.

Furthermore, the susceptibility diagram shows that the dual-peak feature can be easily observed for  $\text{Cd}_3\text{As}_2$  with its intrinsic Fermi level,  $\varepsilon_{F0}$ . Not only does  $\text{Cd}_3\text{As}_2$  have

the largest green ( $\varepsilon_{F0}$ ) region, it also have a very noticeable shift in Fig. 3(a), which is further supported by Fig. 2, where it can exhibits this feature more prominently. This is due to  $\text{Cd}_3\text{As}_2$  having high  $\varepsilon_{F0}$  as compared to the other three topological semimetals. Thus, the susceptibility diagram shows that  $\text{Cd}_3\text{As}_2$  is a suitable candidate amongst these four topological semimetals to observe this dual-peak feature in future experiments.

## C. Emission current density and scaling law

For comparison, the thermal-field emission current density between DSM/WSM [ $\mathcal{J}_{\perp}$  in Eq. (15)] and traditional materials with parabolic dispersion [Eq. (12)] is plotted in Fig. 4(a) at  $T = 700$  K and Fig. 4(b) 2.5 V/nm at its intrinsic Fermi level,  $\varepsilon_{F0}$ . Due to the semi-metallic nature of DSMs/WSMs, it is expected that they exhibit a lower emission current density than the metallic emitters due to their limited electronic carrier density. Indeed, we observe that the emission current density ( $\mathcal{J}_{\perp}$ ) of DSMs/WSMs [ $\text{Cd}_3\text{As}_2$  (red line),  $\text{TaAs}$  (green line) and  $\text{TaP}$  (orange line)] is lower than traditional materials [ $\text{W}$  (yellow line) and  $\text{Pt}$  (brown line)] with the exception of  $\text{Na}_3\text{Bi}$  (blue line) due to its significant lower work function of 2.35 eV. Such behaviour is expected from Eqs. (12) and (15) as they share similar  $F$  and  $T$  dependence terms in their thermal-field emission current densities.

Interestingly, the inset in Fig. 4(a) shows that the field emission follows an unconventional scaling of  $\ln(J/F^3) \propto -1/F$  (Eq. (20)) for all topological semimetals. The excellent linearity of  $\ln(J/F^3) \propto -1/F$  reveals that DSM/WSM emitter follows an unconventional non-FN scaling not commonly seen in traditional materials.

The effects of the parameters  $\varepsilon_F$  on the ratio of  $\mathcal{J}_{\perp}^{\text{SM}}(\varepsilon_F)$  against  $\mathcal{J}_{\perp}^{\text{SM}}(\varepsilon_{F0})$  while varying  $F$  and  $T$  are being investigated in Figs. 4(c) and 4(d). The ratio dips below 1 for increasing  $F$  / decreasing  $T$ . With a lower  $\varepsilon_F$ , it is easier to activate more low energy carriers for emission as compared to a higher  $\varepsilon_F$  with an enlarged conduction band when increasing  $F$ . Similarly, the reduced number of high energy carriers has a lesser effect on the TED as with a lower  $\varepsilon_F$ , the emission is dominated by low energy carriers. This goes in tandem with the loss of the dual-peak feature, which signifies the dominance of the low energy carriers for  $\varepsilon_{F0}$  as seen either fixing  $T = 700$  K or 2.5 V/nm in Fig. 3. Notably,  $\text{Na}_3\text{Bi}$  exceed 1 in Fig. 4(c), which is expected as it did not exhibit the dual-peak property with  $\varepsilon_{F0}$  as seen in Figs. 2 and 3. Thus, a higher thermal-field emission current densities can be achieved by either altering  $\varepsilon_F$  or by manipulating the dual-peak feature with the variation of  $F$  and  $T$ .

#### IV. CONCLUSION

In conclusion, we have developed a thermal-field emission model for 3D Dirac semimetal (DSM) and Weyl semimetal (WSM) with a linear Dirac conic energy dispersion such as Cd<sub>3</sub>As<sub>2</sub>, Na<sub>3</sub>Bi, TaAs, and TaP. Our results predict the existence of a non-trivial dual-peak feature in the total energy distribution (TED) and a new  $\ln(J/F^3) \propto -1/F$  scaling law, which is absent in an electron field emitter composed of traditional metals with conventional 3D parabolic energy band structure. The characteristics of this dual-peak feature are unique to DSM/WSM and may serve as a smoking gun signature for the Dirac conic energy dispersion in topological semimetals. Furthermore, the relatively low work function of Na<sub>3</sub>Bi can be beneficial for field emission application due to its high emission current density. Cd<sub>3</sub>As<sub>2</sub> with its sufficiently high Fermi level (in spite of high work function), is also a suitable candidate for achieving a larger emission current density by exploiting the high sensitivity of the dual-peak feature with the variation of  $F$ ,  $T$  and  $\varepsilon_F$ . Finally, we remark that our model does not capture secondary effects, such as field-induced topological phase transition [9, 13, 63], band bending [64], space charge [65, 66], and Fermi velocity shifting [58, 67]. Such effects could be included in future works to investigate their roles on the thermal-field emission characteristics of 3D DSM/WSM.

#### V. ACKNOWLEDGEMENTS

This work is funded by MOE Tier 2 (2018-T2-1-007). Y.S.A. acknowledges the support of SUTD Startup Research Grant (Project No. SRT3CI21163). W.J.C. acknowledges MOE PhD RSS.

#### Appendix A: Derivation of TED and emission current density with linear (non-parabolic) dispersion for a DSM/WSM

The generalised emission electrical current density from a 3D bulk electron emitter with a linear (non-parabolic) dispersion is shown in Eq. (5) of Section II as

$$\mathcal{J}_\perp^L = \frac{e}{2\pi\hbar} \left( \int f(\varepsilon_{\mathbf{k}}) \mathcal{T}(\varepsilon_\perp) \Lambda_\perp d\varepsilon_\perp \right) \times \left( \iint \frac{g}{(2\pi)^2} \Lambda_\parallel^{-1} d\phi_{\mathbf{k}_\parallel} d\varepsilon_\parallel \right), \quad (\text{A1})$$

where the superscript  $L$  indicates a linear dispersion. Inserting Eq. (10) into Eq. (5) garner us Eq. (14) such that,

$$\mathcal{J}_\perp^{\text{SM}} = \sum_{a=1}^N \frac{g_a e}{(2\pi\hbar)^3} \left( \int |\varepsilon_{\perp,a}| \mathcal{T}(\varepsilon_{\perp,a}) f(\varepsilon_{\mathbf{k},a}) d\varepsilon_{\perp,a} \right) \times \left( \iint \frac{\varepsilon_{\parallel,a}}{\tilde{v}_a^2} d\phi_{\mathbf{k}_\parallel,a} d\varepsilon_{\mathbf{k},a} \right). \quad (\text{A2})$$

Without loss of generality, we can discard the Dirac node label,  $a$  by specifying a Dirac node. This allow us to temporary remove the summation, which can be placed back at the end.

The  $\varepsilon_\perp$  integration then gives:

$$\int |\varepsilon_\perp| \mathcal{T}(\varepsilon_\perp) d\varepsilon_\perp = \frac{D_F}{\hbar\varepsilon_{\mathbf{k}}} \int_{-\infty}^{\varepsilon_{\mathbf{k}}} |\varepsilon_\perp| e^{(\varepsilon_\perp - \varepsilon_F)/d_F} d\varepsilon_\perp, \quad (\text{A3})$$

where the approximation ( $0 \rightarrow -\infty$ ) can be made as the emission takes place near the Fermi level.

Due to the absolute function in  $\varepsilon_\perp$ , we have to consider both the  $\varepsilon_{\mathbf{k}} < 0$  and  $\varepsilon_{\mathbf{k}} > 0$  regime, such that for  $\varepsilon_{\mathbf{k}} < 0$ ,

$$\int_{-\infty}^{\varepsilon_{\mathbf{k}}} |\varepsilon_\perp| e^{(\varepsilon_\perp - \varepsilon_F)/d_F} d\varepsilon_\perp = d_F^2 \exp\left\{ \frac{\varepsilon_{\mathbf{k}} - \varepsilon_F}{d_F} \right\} \left( 1 - \frac{\varepsilon_{\mathbf{k}}}{d_F} \right), \quad (\text{A4})$$

and for  $\varepsilon_{\mathbf{k}} > 0$ ,

$$\int_{-\infty}^{\varepsilon_{\mathbf{k}}} |\varepsilon_\perp| e^{(\varepsilon_\perp - \varepsilon_F)/d_F} d\varepsilon_\perp = d_F^2 \exp\left\{ -\frac{\varepsilon_F}{d_F} \right\} \times \left( 2 + \left( \frac{\varepsilon_{\mathbf{k}}}{d_F} - 1 \right) \exp\left\{ \frac{\varepsilon_{\mathbf{k}}}{d_F} \right\} \right). \quad (\text{A5})$$

Hence, we can combine them into a dimensionless tunnelling function such that

$$\lambda(\varepsilon_{\mathbf{k}}/d_F) = \exp\left\{ \frac{\varepsilon_{\mathbf{k}}}{d_F} \right\} \left( \frac{\varepsilon_{\mathbf{k}}}{d_F} - 1 \right) \text{sign}(\varepsilon_{\mathbf{k}}) + 1 + \text{sign}(\varepsilon_{\mathbf{k}}) \quad (\text{A6})$$

where

$$\lambda(\varepsilon_{\mathbf{k}}/d_F) = \begin{cases} \left( 1 - \frac{\varepsilon_{\mathbf{k}}}{d_F} \right) \exp\left\{ \frac{\varepsilon_{\mathbf{k}}}{d_F} \right\} & , \varepsilon_{\mathbf{k}} < 0 \\ 2 + \left( \frac{\varepsilon_{\mathbf{k}}}{d_F} - 1 \right) \exp\left\{ \frac{\varepsilon_{\mathbf{k}}}{d_F} \right\} & , \varepsilon_{\mathbf{k}} \geq 0. \end{cases}$$

This can be done as the limits of Eqs. (A4) and (A5) at 0 are equal and can be easily verified. Hence, the  $\varepsilon_\perp$  integration becomes

$$\int |\varepsilon_\perp| \mathcal{T}(\varepsilon_\perp) d\varepsilon_\perp = \frac{D_F}{\hbar\varepsilon_{\mathbf{k}}} \lambda(\varepsilon_{\mathbf{k}}/d_F). \quad (\text{A7})$$

Next for the  $\varepsilon_\parallel$  and  $\phi_{\mathbf{k}_\parallel,a}$  integration,

$$\iint \frac{\varepsilon_\parallel}{\tilde{v}^2} d\phi_{\mathbf{k}_\parallel} d\varepsilon_\parallel = \int \frac{2\pi\varepsilon_{\mathbf{k}}}{v_{Fx}v_{Fy}} d\varepsilon_{\mathbf{k}} \quad (\text{A8})$$



where  $\tilde{v} \equiv v_{Fy} \sqrt{(v_{Fx}/v_{Fy})^2 \cos^2 \phi_{\mathbf{k}_{\parallel}} + \sin^2 \phi_{\mathbf{k}_{\parallel}}}$  and the identity,  $\int_0^{2\pi} (a^2 \cos^2 \phi_{\mathbf{k}_{\parallel}} + \sin^2 \phi_{\mathbf{k}_{\parallel}})^{-1} d\phi_{\mathbf{k}_{\parallel}} = 2\pi/a$  and  $\partial\varepsilon_{\mathbf{k}}/\partial\varepsilon_{\parallel} = \varepsilon_{\parallel}/\varepsilon_{\mathbf{k}}$  was used.

This changes Eq. (14) into Eq. (15)

$$\mathcal{J}_{\perp}^{\text{SM}} = \sum_{a=1}^N \frac{c_{\text{SM},a} F^2}{\Phi t^2} D_F \exp\left\{-\frac{\varepsilon_F}{d_F}\right\} \times \int_{-\infty}^{\infty} f(\varepsilon_{\mathbf{k},a}) \lambda(\varepsilon_{\mathbf{k},a}/d_F) d\varepsilon_{\mathbf{k},a}. \quad (\text{A9})$$

where the SM represents the emission current density of a topological semimetal,  $c_{\text{SM}} = e^3 g / 32 m \pi^2 \hbar v_{Fx} v_{Fy}$  is a constant, with  $m_e$  being the rest mass of the electron.

The TED can be extracted from the emission current density from

$$P(\varepsilon_{\mathbf{k}}) = \frac{\partial \mathcal{J}_{\perp}}{\partial \varepsilon_{\mathbf{k}}}, \quad (\text{A10})$$

which gives us a general form:

$$P(\varepsilon_{\mathbf{k}}) = \frac{e}{2\pi \hbar^3} f(\varepsilon_{\mathbf{k}}) \int \mathcal{T}(\varepsilon_{\perp}) \Lambda_{\perp} D(\varepsilon_{\mathbf{k}}) d\varepsilon_{\perp} d\phi_{\mathbf{k}_{\parallel}}. \quad (\text{A11})$$

For DSMs/WSMs, we can apply the results from the various integration in Eqs. (A7) and (A8) and Eq. (10) to obtain the TED in Eq. (23) such that,

$$P^{\text{SM}}(\varepsilon_{\mathbf{k}}) = \sum_{a=1}^N \frac{c_{\text{SM},a} F^2}{\Phi t^2} D_F \exp\left\{-\frac{\varepsilon_F}{d_F}\right\} \times f(\varepsilon_{\mathbf{k},a}) \lambda(\varepsilon_{\mathbf{k},a}/d_F). \quad (\text{A12})$$

- 
- [1] Y.-W. Son, M. L. Cohen, and S. G. Louie, Energy Gaps in Graphene Nanoribbons, *Phys. Rev. Lett.* **97**, 216803 (2006), arXiv:0611602 [cond-mat].
- [2] T. Oka and H. Aoki, Photovoltaic Hall effect in Graphene, *Phys. Rev. B* **79**, 081406 (2009), arXiv:0807.4767.
- [3] G. Xu *et al.*, Chern Semimetal and the Quantized Anomalous Hall Effect in  $\text{HgCr}_2\text{Se}_4$ , *Phys. Rev. Lett.* **107**, 186806 (2011).
- [4] B. Q. Lv *et al.*, Observation of Weyl nodes in TaAs, *Nat. Phys.* **11**, 724 (2015).
- [5] T. M. McCormick, I. Kimchi, and N. Trivedi, Minimal models for topological Weyl semimetals, *Phys. Rev. B* **95**, 075133 (2017).
- [6] Z. K. Liu *et al.*, A stable three-dimensional topological Dirac semimetal  $\text{Cd}_3\text{As}_2$ , *Nat. Mater.* **13**, 677 (2014).
- [7] Z. K. Liu *et al.*, Discovery of a Three-Dimensional Topological Dirac Semimetal,  $\text{Na}_3\text{Bi}$ , *Science* **343**, 864 (2014).
- [8] I. Crassee *et al.*, 3D Dirac semimetal  $\text{Cd}_3\text{As}_2$ : A review of material properties, *Phys. Rev. Mater.* **2**, 120302 (2018), arXiv:1810.03726.
- [9] T. Wehling, A. Black-Schaffer, and A. Balatsky, Dirac materials, *Adv. Phys.* **63**, 1 (2014), arXiv:1405.5774.
- [10] E. McCann and M. Koshino, The electronic properties of bilayer graphene, *Reports Prog. Phys.* **76**, 056503 (2013), arXiv:1205.6953.
- [11] X. Wan, A. M. Turner, A. Vishwanath, and S. Y. Savrasov, Topological semimetal and Fermi-arc surface states in the electronic structure of pyrochlore iridates, *Phys. Rev. B* **83**, 205101 (2011).
- [12] J. Xiong *et al.*, Anomalous conductivity tensor in the Dirac semimetal  $\text{Na}_3\text{Bi}$ , *EPL (Europhysics Lett.)* **114**, 27002 (2016), arXiv:1502.06266.
- [13] S. Wang *et al.*, Quantum transport in Dirac and Weyl semimetals: a review, *Adv. Phys. X* **2**, 518 (2017).
- [14] M. Lasia and L. Brey, Optical properties of magnetically doped ultrathin topological insulator slabs, *Phys. Rev. B* **90**, 075417 (2014), arXiv:1404.7040.
- [15] B. Xu *et al.*, Optical spectroscopy of the Weyl semimetal TaAs, *Phys. Rev. B* **93**, 121110 (2016).
- [16] S. Polatkan *et al.*, Magneto-Optics of a Weyl Semimetal beyond the Conical Band Approximation: Case Study of TaP, *Phys. Rev. Lett.* **124**, 176402 (2020), arXiv:1912.07327.
- [17] Y. H. Choi *et al.*, Transport and magnetic properties of Cr-, Fe-, Cu-doped topological insulators, *J. Appl. Phys.* **109**, 07E312 (2011).
- [18] P.-B. Li, Z.-L. Xiang, P. Rabl, and F. Nori, Hybrid Quantum Device with Nitrogen-Vacancy Centers in Diamond Coupled to Carbon Nanotubes, *Phys. Rev. Lett.* **117**, 015502 (2016), arXiv:1606.02998.
- [19] C. Zhu *et al.*, A robust and tuneable mid-infrared optical switch enabled by bulk Dirac fermions, *Nat. Commun.* **8**, 14111 (2017).
- [20] Q. Wang *et al.*, Ultrafast Broadband Photodetectors Based on Three-Dimensional Dirac Semimetal  $\text{Cd}_3\text{As}_2$ , *Nano Lett.* **17**, 834 (2017).
- [21] L. Šmejkal, Y. Mokrousov, B. Yan, and A. H. MacDonald, Topological antiferromagnetic spintronics, *Nat. Phys.* **14**, 242 (2018).
- [22] A. B. Khanikaev *et al.*, Photonic topological insulators, *Nat. Mater.* **12**, 233 (2013).
- [23] Y.-Z. Yu *et al.*, Photonic topological semimetals in bianisotropic metamaterials, *Sci. Rep.* **9**, 18312 (2019).
- [24] J. Lim, Y. S. Ang, F. J. García de Abajo, I. Kaminer, L. K. Ang, and L. J. Wong, Efficient generation of extreme terahertz harmonics in three-dimensional Dirac semimetals, *Phys. Rev. Res.* **2**, 043252 (2020).
- [25] T. Zhang, K. J. A. Ooi, W. Chen, L. K. Ang, and Y. Sin Ang, Optical Kerr effect and third harmonic generation in topological Dirac/Weyl semimetal, *Opt. Express* **27**, 38270 (2019).
- [26] J. Lim, K. J. A. Ooi, C. Zhang, L. K. Ang, and Y. S. Ang, Broadband strong optical dichroism in topological Dirac semimetals with Fermi velocity anisotropy, *Chinese Phys. B* **29**, 077802 (2020).

- [27] A.-Q. Wang, X.-G. Ye, D.-P. Yu, and Z.-M. Liao, Topological Semimetal Nanostructures: From Properties to Topotronics, *ACS Nano* **14**, 3755 (2020).
- [28] S. Hofmann, C. Ducati, B. Kleinsorge, and J. Robertson, Direct growth of aligned carbon nanotube field emitter arrays onto plastic substrates, *Appl. Phys. Lett.* **83**, 4661 (2003).
- [29] S.-D. Liang and L. Chen, Generalized Fowler-Nordheim Theory of Field Emission of Carbon Nanotubes, *Phys. Rev. Lett.* **101**, 027602 (2008).
- [30] S. Zhou *et al.*, Ultrafast Field-Emission Electron Sources Based on Nanomaterials, *Adv. Mater.* **31**, 1 (2019).
- [31] F. Giubileo *et al.*, Field Emission from Carbon Nanostructures, *Appl. Sci.* **8**, 526 (2018).
- [32] L. Chen *et al.*, Graphene field emitters: A review of fabrication, characterization and properties, *Mater. Sci. Eng. B* **220**, 44 (2017).
- [33] S. Sun, L. K. Ang, D. Shiffler, and J. W. Luginsland, Klein tunnelling model of low energy electron field emission from single-layer graphene sheet, *Appl. Phys. Lett.* **99**, 013112 (2011).
- [34] Y. Ang, S.-J. Liang, and L. Ang, Theoretical modeling of electron emission from graphene, *MRS Bull.* **42**, 505 (2017).
- [35] X. Wei, Y. Bando, and D. Golberg, Electron emission from individual graphene nanoribbons driven by internal electric field, *ACS Nano* **6**, 705 (2012).
- [36] S.-J. Liang and L. K. Ang, Electron thermionic emission from graphene and a thermionic energy converter, *Phys. Rev. Applied* **3**, 014002 (2015).
- [37] Y. S. Ang, H. Y. Yang, and L. K. Ang, Universal scaling laws in schottky heterostructures based on two-dimensional materials, *Phys. Rev. Lett.* **121**, 056802 (2018).
- [38] Y. S. Ang, Y. Chen, C. Tan, and L. K. Ang, Generalized high-energy thermionic electron injection at graphene interface, *Phys. Rev. Applied* **12**, 014057 (2019).
- [39] S. Huang, M. Sanderson, Y. Zhang, and C. Zhang, High efficiency and non-Richardson thermionics in three dimensional Dirac materials, *Appl. Phys. Lett.* **111**, 1 (2017).
- [40] Y. S. Ang, L. Cao, and L. K. Ang, Physics of electron emission and injection in two-dimensional materials: Theory and simulation, *InfoMat*, 502 (2021).
- [41] R. G. Forbes, Simple good approximations for the special elliptic functions in standard Fowler-Nordheim tunneling theory for a Schottky-Nordheim barrier, *Appl. Phys. Lett.* **89**, 113122 (2006).
- [42] R. G. Forbes and J. H. Deane, Reformulation of the standard theory of Fowler-Nordheim tunnelling and cold field electron emission, *Proc. R. Soc. A Math. Phys. Eng. Sci.* **463**, 2907 (2007).
- [43] K. L. Jensen and M. Cahay, General thermal-field emission equation, *Appl. Phys. Lett.* **88**, 10 (2006).
- [44] L. W. Swanson, L. C. Crouser, and F. M. Charbonnier, Energy exchanges attending field electron emission, *Phys. Rev.* **151**, 327 (1966).
- [45] M. Dionne, S. Coulombe, and J.-L. Meunier, Energy exchange during electron emission from carbon nanotubes: Considerations on tip cooling effect and destruction of the emitter, *Phys. Rev. B* **80**, 085429 (2009).
- [46] M. S. Chung, Energy exchange processes in electron emission at high fields and temperatures, *J. Vac. Sci. Technol. B Microelectron. Nanom. Struct.* **12**, 727 (1994).
- [47] V. T. Binh, N. Garcia, and S. Purcell, *Electron Field Emission from Atom-Sources: Fabrication, Properties, and Applications of Nanotips*, in *Adv. Imaging Electron Phys.*, Vol. 95 (Elsevier, 1996) pp. 63–153.
- [48] R. D. Young, Theoretical Total-Energy Distribution of Field-Emitted Electrons, *Phys. Rev.* **113**, 110 (1959).
- [49] J. W. Gadzuk and E. W. Plummer, Field Emission Energy Distribution (FEED), *Rev. Mod. Phys.* **45**, 487 (1973).
- [50] J. Lee *et al.*, High-performance field emission from a carbon nanotube carpet, *Carbon N. Y.* **50**, 3889 (2012).
- [51] N. de Jonge, M. Allieux, J. T. Oostveen, K. B. K. Teo, and W. I. Milne, Optical Performance of Carbon-Nanotube Electron Sources, *Phys. Rev. Lett.* **94**, 186807 (2005).
- [52] L. Li, W. Sun, S. Tian, X. Xia, J. Li, and C. Gu, Floral-clustered few-layer graphene nanosheet array as high performance field emitter, *Nanoscale* **4**, 6383 (2012).
- [53] E. L. Murphy and R. H. Good, Thermionic Emission, Field Emission, and the Transition Region, *Phys. Rev.* **102**, 1464 (1956).
- [54] G. S. Jenkins, C. Lane, B. Barbiellini, A. B. Sushkov, R. L. Carey, F. Liu, J. W. Krizan, S. K. Kushwaha, Q. Gibson, T.-r. Chang, H.-t. Jeng, H. Lin, R. J. Cava, A. Bansil, and H. D. Drew, Three-dimensional Dirac cone carrier dynamics in  $\text{Na}_3\text{Bi}$  and  $\text{Cd}_3\text{As}_2$ , *Phys. Rev. B* **94**, 085121 (2016).
- [55] Z. Huang *et al.*, High responsivity and fast UV–vis–short-wavelength IR photodetector based on  $\text{Cd}_3\text{As}_2 / \text{MoS}_2$  heterojunction, *Nanotechnology* **31**, 064001 (2020).
- [56] C.-C. Lee *et al.*, Fermi surface interconnectivity and topology in Weyl fermion semimetals TaAs, TaP, NbAs, and NbP, *Phys. Rev. B* **92**, 235104 (2015).
- [57] S. Chi *et al.*, Ultra-broadband photodetection of weyl semimetal taas up to infrared 10  $\mu\text{m}$  range at room temperature (2017), [arXiv:1705.05086 \[cond-mat.mtrl-sci\]](https://arxiv.org/abs/1705.05086).
- [58] D. Grassano, O. Pulci, A. Mosca Conte, and F. Bechstedt, Validity of Weyl fermion picture for transition metals mononpnictides TaAs, TaP, NbAs, and NbP from ab initio studies, *Sci. Rep.* **8**, 3534 (2018).
- [59] Z. Du *et al.*, Field emission behaviors of CsPbI 3 nanobelts, *J. Mater. Chem. C* **8**, 5156 (2020).
- [60] T. Berry, L. A. Pressley, W. A. Phelan, T. T. Tran, and T. M. McQueen, Laser-Enhanced Single Crystal Growth of Non-Symmorphic Materials: Applications to an Eight-Fold Fermion Candidate, *Chem. Mater.* **32**, 5827 (2020).
- [61] N. Nicolaou and A. Modinos, Band-structure effects in field-emission energy distributions in tungsten, *Phys. Rev. B* **11**, 3687 (1975).
- [62] A. K. Bordoloi and S. Auluck, Electronic structure of platinum, *J. Phys. F Met. Phys.* **13**, 2101 (1983).
- [63] N. P. Armitage, E. J. Mele, and A. Vishwanath, Weyl and Dirac semimetals in three-dimensional solids, *Rev. Mod. Phys.* **90**, 015001 (2018), [arXiv:1705.01111](https://arxiv.org/abs/1705.01111).
- [64] V. Litovchenko, A. Evtukh, *et al.*, Electron field emission from narrow band gap semiconductors (InAs), *Semicond. Sci. Technol.* **22**, 1092 (2007).
- [65] K. A. Abdul Khalid, T. J. Leong, and K. Mohamed, Review on Thermionic Energy Converters, *IEEE Trans. Electron Devices* **63**, 2231 (2016).
- [66] P. Zhang, Y. S. Ang, A. L. Garner, Á. Valfells, J. W. Luginsland, and L. K. Ang, Space-charge limited current in nanodiodes: Ballistic, collisional, and dynamical effects,

- J. Appl. Phys. **129**, 100902 (2021).
- [67] Y. Baba, Á. Díaz-Fernández, E. Díaz, F. Domínguez-Adame, and R. A. Molina, Electric field manipulation of surface states in topological semimetals, *Phys. Rev. B* **100**, 165105 (2019), [arXiv:1907.06516](https://arxiv.org/abs/1907.06516).